Research Square

Preprints are preliminary reports that have not undergone peer review.
They should not be considered conclusive, used to inform clinical practice,
or referenced by the media as validated information.

Self-assembled polysaccharide nanoparticles enable M cell–mediated oral immune entry and enhance systemic antitumor immunity

Zheming Hu
Beijing University of Chinese Medicine
Qin Zhang
Beijing University of Chinese Medicine
Haojie Wang
Beijing University of Chinese Medicine
Wulong Wen
Beijing University of Chinese Medicine
Lingfan Fan
Beijing University of Chinese Medicine
Jinxuan Yang
Beijing University of Chinese Medicine
Shuhui Geng
Beijing University of Chinese Medicine
Lan Qin
Beijing University of Chinese Medicine
Fengyi Ma
Beijing University of Chinese Medicine
Yang Lu
luyang@bucm.edu.cn

Beijing University of Chinese Medicine

Research Article

Keywords: Ginseng polysaccharide, Chito-oligosaccharide, self-assembly, Oral delivery, M-cell targeting, Radio-immunotherapy

Posted Date: April 14th, 2026

DOI: https://doi.org/10.21203/rs.3.rs-9324515/v1

License: This work is licensed under a Creative Commons Attribution 4.0 International License.
Read Full License

Additional Declarations: No competing interests reported.

Abstract

Oral delivery of immunomodulators offers a non-invasive strategy for sustained immune intervention, yet its application to macromolecular agents remains limited by the lack of defined immune entry pathways. In particular, whether orally administered biomacromolecules can access organized intestinal lymphoid tissues and contribute to systemic immunity remains poorly understood. Here, we report a structure-guided polysaccharide assembly (COS@GP) that enables pathway-defined oral immune entry via M cell–mediated transcytosis into Peyer's patches. The co-assembled architecture maintains structural integrity under gastrointestinal conditions while promoting coordinated cellular uptake. Using an in vitro M-cell model and in vivo analysis, COS@GP exhibits enhanced trans-epithelial transport and preferential accumulation within intestinal lymphoid tissues. At the biological level, COS@GP induces a controlled mucosal immune activation characterized by the upregulation of innate immune pathways without excessive inflammatory responses. This localized priming facilitates downstream immune propagation and enhances systemic antitumor immunity when combined with radiotherapy. Collectively, this study establishes a structure-function framework in which polysaccharide assemblies are engineered not only for delivery, but for defining immune entry pathways, providing a foundation for oral immunomodulatory strategies.

1. Introduction

Cancer immunotherapy increasingly relies on sustained modulation of the immune system rather than transient intervention [1–3]. While immune checkpoint inhibitors have demonstrated clinical success, their administration is largely restricted to parenteral routes, which limits long-term accessibility and may lead to systemic adverse effects [4–6]. In this context, oral delivery represents an attractive alternative for repeated and patient-compliant immune modulation [7]. However, the oral delivery of macromolecular immunomodulators remains fundamentally constrained [8]. Beyond gastrointestinal degradation, a more critical limitation lies in the absence of defined pathways that enable these agents to access organized intestinal lymphoid tissues, such as Peyer's patches [9–11]. Without engaging these specialized immune inductive sites, orally administered macromolecules are unlikely to contribute to systemic immune activation.

Polysaccharides have emerged as promising immunomodulatory candidates due to their intrinsic bioactivity and biocompatibility. Among them, chitosan oligosaccharide (COS) and ginseng polysaccharides (GP) have been widely reported to activate innate and adaptive immune responses [12, 13]. Yet, their oral application is often associated with heterogeneous outcomes, largely attributed to indirect effects such as microbiota modulation and nonspecific mucosal responses [14, 15] and poorly defined uptake processes. This lack of mechanistic clarity is closely linked to their structural instability, as freely dispersed polysaccharides fail to maintain defined architectures under gastrointestinal conditions, resulting in unpredictable immune engagement [16, 17]. Consequently, despite their biological potential, polysaccharides remain difficult to rationally engineer as precision oral immunomodulatory systems [18].

To address these challenges, oral delivery systems must be designed not only to protect therapeutic components from gastrointestinal degradation, but also to enable their access to intestinal immune inductive sites. Such systems should integrate structural stability with immunological functionality, allowing coordinated presentation of immune-active signals at defined sampling interfaces [19]. In this context, the selection of carrier materials becomes critical, as the delivery platform itself can influence the initiation of immune responses [20].

In this study, COS was selected not only as a cationic scaffold but also as a functional immunomodulatory component. Although COS has been reported to engage innate immune sensing pathways, its free oral application is limited by short intestinal residence time and the lack of active transport mechanisms to organized lymphoid tissues such as Peyer's patches [21]. Peyer's patches function as key mucosal inductive sites where antigen sampling initiates systemic immune priming. We therefore hypothesized that integrating COS with GP into a self-assembled nanostructure through intermolecular interactions could enable coordinated delivery of structural support and immune signals. This co-assembly was designed to prevent premature dissociation and facilitate synchronized immune activation within the same microenvironment.

Radiotherapy (RT) provides a clinically relevant context in which this strategy can be evaluated. Although RT induces immunogenic cell death and localized inflammatory signaling, these effects often fail to generate durable systemic immune responses [22, 23]. This limitation highlights the need for complementary approaches that enhance systemic immune readiness through anatomically distinct immune interfaces. Here, we report a self-assembled COS@GP nanoparticle system that establishes a pathway-defined oral immune entry through M cell–mediated transcytosis into Peyer's patches. This system supports localized innate immune sensing, potentially involving the cGAS-STING axis, and enhances systemic antitumor immunity and remodels the tumor immune microenvironment when combined with radiotherapy [24–26]. Collectively, this study establishes a structure-guided polysaccharide system that links oral delivery with defined immune entry pathways, providing a framework for polysaccharide-enabled immunotherapy.

2. Materials and methods

2.1 Materials and reagents

Ginseng polysaccharides (GP, purity > 98%) were sourced from Yangling Ciyuan Biotechnology (Shanxi, China). Chitosan oligosaccharide (COS, Mw < 3000 Da) and K-R buffer were supplied from Yuanye Bio-Technology (Shanghai, China). Chemical reagents including sodium tripolyphosphate (TPP), fluorescein isothiocyanate (FITC), and rhodamine B were purchased from Aladdin (Shanghai, China). Enzyme-linked immunosorbent assay (ELISA) kits for mouse interleukin-6 (IL-6), tumor necrosis factor-alpha (TNF-α), and interferon-gamma (IFN-γ) were purchased from Meimian Industrial (Jiangsu, China). Cell Counting Kit-8 (CCK-8) was provided by LABLED Inc. (Beijing, China), Transwell® permeable inserts (0.4 μm pore size, 12-well) were obtained from Corning (USA). Phosphate-buffered saline (PBS, pH 7.4) and other cell

culture essentials, such as Trypsin-EDTA and penicillin-streptomycin were acquired from Gibco (USA). All other chemical reagents were of analytical grade and used as received.

2.2 Cell lines

The murine mammary carcinoma cell line 4T1, murine dendritic cell line DC2.4, and human Raji B cells were purchased from Pricella (Wuhan, China). These cells were maintained in RPMI-1640 medium (Gibco, USA) supplemented with 10% fetal bovine serum (FBS) (Corning, USA). The human intestinal epithelial cell line Caco-2, human goblet cell line HT29-MTX-E12, and murine macrophage cell line RAW 264.7 were cultured in DMEM (Gibco, USA) containing 10% or 15% (for Caco-2) FBS.

All culture media were fortified with 100 U/mL penicillin and 100 μg/mL streptomycin. Cells were incubated at 37°C in a humidified atmosphere with 5% CO_2. For transport studies, Caco-2, HT29-MTX-E12, and Raji B cells were used to construct the in vitro triple-culture intestinal model as described in Section 2.8.

2.3 Mice

Female Balb/c mice (6–8 weeks old, weighing 18–20 g) and male Wistar rats (8–10 weeks old, weighing 220–250 g) were purchased from Beijing Vital River Laboratory Animal Technology (Beijing, China). Animals were housed under specific pathogen-free (SPF) conditions with a 12-hour light/dark cycle at a controlled temperature of 25 ± 2°C and 50 ± 10% humidity, with free access to food and water.

All animal experimental protocols were reviewed and approved by the Institutional Animal Care and Use Committee (IACUC) of Beijing University of Chinese Medicine (Approval No. BUCM20250724-002 and BUCM20250814-003). All procedures were performed in strict accordance with the Guide for the Care and Use of Laboratory Animals.

2.4 Preparation and characterization of COS@GP

2.4.1 Structural analysis of GP

The homogeneity and absolute molecular weight of GP were determined using size exclusion chromatography coupled with multi-angle laser light scattering and refractive index detection (SEC-MALLS-RI). The weight-average molecular weight (M_w), number-average molecular weight (M_n), and polydispersity index (M_w/M_n) were measured on a DAWN HELEOS-II laser photometer (Wyatt Technology, USA) equipped with tandem columns (Shodex OH-pak SB-805 and 803) at 45°C. The mobile phase (0.1 M $NaNO_3$ with 0.02% NaN_3) was delivered at 0.6 mL/min. An Optilab T-rEX differential refractive index detector (Wyatt Technology) was used to determine the concentration and the dn/dc value, which was set at 0.141 mL/g.

For monosaccharide composition, GP was analyzed via pre-column derivatization with 1-phenyl-3-methyl-5-pyrazolone (PMP). The analysis was performed on a Shimadzu LC-20AD HPLC system using an

Xtimate C18 column (4.6×200 mm, 5 μm). Elution was monitored at 250 nm, and monosaccharides were identified and quantified against standard reference sugars.

2.4.2 Preparation and formulation optimization of COS@GP

The COS@GP were fabricated via a coordinated process of electrostatic self-assembly and ionic gelation. Briefly, the GP concentrated solution was introduced dropwise into a COS aqueous solution under magnetic stirring (500 rpm) to induce intermolecular nucleation driven by charge neutralization. Subsequently, a TPP solution (1.0 mg/mL) incorporated as an ionic crosslinker to bridge the polysaccharide chains and stabilize the emerging nanostructures.

To identify the optimal formulation, a Plackett-Burman (PB) screening design was employed to evaluate the influence of three critical variables: the concentrations of COS, GP, and TPP. Twelve experimental runs were performed as detailed in Table S3. The selection of the optimal formulation was based on a comprehensive assessment of the hydrodynamic diameter, polydispersity index, and zeta potential. Based on the PB matrix results, the formulation yielding the most favorable physicochemical properties was utilized for all subsequent experiments.

2.4.3 Synthesis of fluorescently labeled COS@GP

To facilitate bio-distribution and transport studies, GP and COS were fluorescently labeled with FITC and Rhodamine B, respectively. FITC-GP was synthesized via L-tyrosine-mediated amination and subsequent reduction with sodium cyanoborohydride, followed by reaction with FITC under alkaline conditions. RhB-COS was prepared by reacting COS with Rhodamine B at pH 5.6 and 37°C overnight. Both polymers were purified by extensive dialysis and ethanol precipitation before lyophilization [27, 28].

To quantify the labeling efficiency and support downstream concentration calculations, a FITC standard curve was established. A series of FITC working solutions (0.1-5.0 μg/mL) were prepared in PBS, and the fluorescence intensity was measured (λ_{ex} = 495 nm, λ_{em} = 525 nm, slit width = 2 nm). The fluorescence labeling efficiency was determined by dissolving 1.0 mg of FITC-GP in PBS and back-calculating its concentration against the regression equation. Dual-labeled nanoparticles (RhB-COS@FITC-GP) were prepared by substituting labeled precursors into the optimized formulation described in Section 2.4.2.

2.4.4 Characterization of COS@GP

The morphology of COS@GP was observed using transmission electron microscopy (TEM, Talos F200x, Thermo Fisher Scientific, USA). The hydrodynamic diameter, polydispersity index (PDI), and zeta potential were determined via dynamic light scattering (DLS) using a Zetasizer Nano ZS (Malvern Panalytical, UK).

To verify the chemical structures and functional groups, Fourier transform infrared (FT-IR) spectra were recorded on a Nicolet spectrometer (Thermo Fisher Scientific, USA) over a range of 4000–400 cm^{-1}. Furthermore, Raman spectra were acquired using a LabRAM HR Evolution Raman spectrometer (Horiba,

Japan) with a 1064 nm excitation laser. The spectra were recorded in the range of 100–3500 cm^{-1} to investigate the vibrational modes and interfacial interactions within the self-assembled nanoparticles. To resolve overlapping vibrational bands and elucidate the specific hydrogen-bonding sites between COS and GP, two-dimensional FTIR correlation spectroscopy (2D-FTIR) correlation spectroscopy was further employed.

2.5 *In vitro* simulated gastrointestinal digestion

To evaluate the structural integrity and stability of COS@GP during oral transit, an in vitro simulated gastrointestinal digestion was performed as previously described with minor modifications [29].

2.5.1 Simulated gastric phase

The COS@GP was mixed with an equal volume of simulated gastric fluid (SGF, pH 1.2) to mimic the dilution and acidic environment of the stomach. The mixture was incubated in a thermostatic shaking water bath at 37°C and 160 rpm to simulate gastric peristalsis. At pre-determined intervals (0, 30, 60, 90, and 120 min), aliquots were withdrawn for analysis, and an equal volume of pre-warmed fresh SGF was replenished to maintain sink conditions.

2.5.2 Simulated intestinal phase

After the 2 h gastric digestion, the resulting chyme was neutralized to pH 6.8 using $NaHCO_3$ to inactivate pepsin and simulate the transition into the duodenum. Subsequently, simulated intestinal fluid (SIF, pH 6.8) was introduced at a volume ratio of 10:3 (gastric chyme to SIF) to initiate the intestinal digestion phase. The process was maintained for an additional 8 hours, with samples collected at 0, 1, 2, 4, 6, and 8 hours. Fresh SIF was replenished after each sampling to maintain the total volume.

2.5.3 Characterization of digestive stability

The physical stability and structural integrity of COS@GP throughout the gastrointestinal transit were monitored by measuring the hydrodynamic diameter and PDI via DLS. Furthermore, to evaluate the protective effect of the nanoparticle architecture against enzymatic degradation, the reducing sugar content in the digestive juices was quantified using a Reducing Sugar Content Assay Kit (Solarbio, China). Free GP served as a control to demonstrate the enhanced stability provided by the COS-based nanocarrier.

2.6 *In vitro* cytotoxicity

To assess the biocompatibility of the synthesized nanoparticles, the cytotoxicity of free GP and COS@GP was evaluated across multiple cell lines, including 4T1, DC2.4, RAW 264.7, and Caco-2, using the CCK-8 assay. Briefly, cells were seeded in 96-well plates at a density of 5×10^3 cells/well and allowed to adhere for 24 h. The cells were then incubated with varying concentrations of free GP or COS@GP (up to 1000 μg/mL) for 24 h. Subsequently, CCK-8 reagent was added and incubated for 2 h. The absorbance

was measured at 450 nm using a microplate reader (Epoch, BioTek, USA). Cell viability was expressed as a percentage relative to the untreated control group.

2.7 Cellular uptake of COS@GP by Caco-2, DC2.4, and 4T1

The intracellular localization of COS@GP was visualized in 4T1, DC2.4 and Caco-2 cells using confocal laser scanning microscopy (CLSM). Briefly, cells were seeded at 1×10^5 cells/dish on glass-bottom dishes and allowed to attach overnight. The cells were then incubated with dual-labeled nanoparticles (RhB-COS@FITC-GP) for 4 h. Following incubation, the cells were washed with PBS, fixed with 4% paraformaldehyde, and counterstained with DAPI to label the nuclei. Confocal images were acquired to assess the internalization and spatial co-localization of the COS and GP components within the cytoplasmic compartment.

To quantify the internalization efficiency across different cell types, 4T1, DC2.4, and Caco-2 cells were incubated with COS@FITC-GP for 4 h at 37°C. After incubation, the cells were harvested, washed with PBS, and resuspended for analysis. Cell viability was monitored using a live/dead dye to ensure the exclusion of debris and dead cells. The fluorescence intensity of 10,000 gated events was measured using a BD FACSCanto II flow cytometer. Data were processed to determine the percentage of positive cells and the mean fluorescence intensity (MFI), reflecting the relative uptake capacity of intestinal, immune, and tumor cells.

2.8 Construction of *in vitro* intestinal epithelial model and transcytosis assay

To evaluate whether the COS@GP could bypass the intestinal epithelial barrier via specialized immune sampling routes, an *in vitro* M-cell-integrated model was constructed to mimic the follicle-associated epithelium (FAE) of Peyer's patches. The *in vitro* intestinal barrier was established by co-culturing Caco-2 and HT29-MTX cells at a 9:1 ratio on Transwell inserts (1.12 cm^2 PET membrane, 0.4 μm pore size) for 14 days, followed by a 7-day induction of M-like cells using Raji B cells (5×10^5 cells/well) in the basolateral chamber according to the previous report [30]. The barrier integrity was validated by TEER values (> 500 $\Omega\cdot cm^2$), and TEM morphological observation. For the transcytosis assay, 500 μL of FITC-GP formulations (500 μg/mL) were added to the apical chamber. At predetermined time intervals (1, 2, and 4 h), samples were collected from the basolateral chamber, and the fluorescence intensity was quantified using a microplate reader to determine the amount of transported nanocarriers.

2.9 In situ single-pass intestinal perfusion (SPIP)

To quantify the intestinal absorption kinetics and evaluate the synergistic effect of the nano-formulation, in situ SPIP was performed on the proximal jejunum of Wistar rats [31]. Briefly, the rats were randomly assigned to groups treated with free GP, the physical mixture of COS/GP, or COS@GP, each at two concentration levels (equivalent to 0.5 mg/mL and 1.0 mg/mL of GP). After the rats were anesthetized, a 15–20 cm jejunal segment was isolated and cannulated. The segments were perfused with the respective formulations at a constant flow rate (Q) of 0.2 mL/min. After reaching a steady state (1 h), the

perfusate was collected at 15 min intervals for 2 h. The absorption rate constant (K_a) and effective permeability coefficient (P_{eff}) were calculated using the concentrations (C_{in}, C_{out}) and volumes (V_{in}, V_{out}) of the perfusate:

$$K_a = \left[1 - \frac{C_{out}}{C_{in}} \bullet \frac{V_{out}}{V_{in}}\right] \bullet \frac{Q}{\pi r^2 L}$$

$$p_{eff} = -\frac{Q}{2\pi rL} \bullet \ln\left(\frac{C_{out}}{C_{in}} \bullet \frac{V_{out}}{V_{in}}\right)$$

2.10 *In vivo* biodistribution and Peyer's patch targeting

The gastrointestinal transit and systemic distribution of COS@GP were monitored using an In Vivo Imaging System (IVIS). Balb/c mice were orally administered with RhB-COS@FITC-GP at a dose of 200 mg/kg, and whole-body fluorescent images were captured at 1, 2, 4, 8, and 12 h post-administration. Subsequently, the mice were sacrificed to harvest major organs and the entire gastrointestinal tract for ex vivo imaging and semi-quantitative radiant efficiency analysis.

To specifically visualize lymphoid targeting, the proximal jejunal segments containing Peyer's patches were resected at the 2 h peak absorption time point and processed into cryosections. To identify M-cell-mediated entry routes, the sections were stained with DyLight 649-labeled Ulex Europaeus Agglutinin I (UEA I) (DL-1068-1, Vector Laboratories) and counterstained with DAPI. The spatial distribution and colocalization of FITC-labeled nanoparticles with UEA I-positive M cells within the FAE were visualized using CLSM.

2.11 In vivo antitumor efficacy

To evaluate the synergistic antitumor efficacy, a subcutaneous 4T1 mammary carcinoma model was established in female Balb/c mice (6 weeks old, 18 ± 2 g). Briefly, 1×10^6 4T1 cells were injected into right dorsal region of the mice. When the tumor volume reached approximately 50 ± 20 mm^3, mice were randomly allocated to experimental groups. Animals were then assigned into six groups: (1) Model (M), (2) COS@GP, (3) Radiotherapy (RT), (4) GP + RT, (5) COS@GP + RT, and (6) COS@GP + RT + FTY720 (to inhibit lymphatic translocation) [32].

On Day 1 (one day post-grouping), mice received a single dose of γ-irradiation (6 Gy) at a dose rate of 1.2 Gy/min using ^{60}Co source (China Institute of Atomic Energy). Prior to irradiation, mice were anesthetized with 1% sodium pentobarbital (10 mg/kg), and lead shielding was applied to protect non-tumor regions. Subsequently, the formulations (equivalent to 200 mg/kg of GP) were administered via daily oral gavage throughout the treatment period. Tumor volumes (V) were monitored every two days and calculated using the formula: $V = (length \times width^2) / 2$. Body weights were also recorded every other day as a measure of systemic toxicity. On Day 14, the experiment was concluded, and the mice were euthanized for subsequent tissue harvesting and analysis.

2.12 Flow cytometric profiling of immune microenvironment

To characterize the immune response, single-cell suspensions from tumors and tumor-draining lymph nodes (TDLNs) were prepared via mechanical dissociation and 70 μm filtration. All cells were initially stained with Zombie NIR™ Fixable Viability Kit (BioLegend, 423105) to exclude dead cells and pre-incubated with anti-mouse CD16/32 (BioLegend, 156405) to block Fc receptors.

For DC maturation in TDLNs, cells were labeled with BV421 anti-CD11c (117343), PE/Cy7 anti-CD80 (104733), and APC anti-CD86 (105011). For intratumoral T cell analysis, viable $CD3^+$ cells (APC anti-CD3, 100235) were gated to identify $CD4^+$ (PerCp/Cy5.5 anti-CD4, 100539) and $CD8^+$ (BV421 anti-CD8α, 100705) effector subsets. To evaluate tumor-associated macrophage (TAM) polarization, single-cell suspensions were stained with BV421 anti-F4/80 (123137) and PE/Cy7 anti-CD80 (104733), followed by fixation, permeabilization, and intracellular staining with PE anti-CD206 (141706). TAMs were identified as $F4/80^+$ cells, and the percentages of M1 ($F4/80^+CD80^+$) and M2 ($F4/80^+CD206^+$) phenotypes were quantified. All data were acquired using a BD FACSCanto II system and analyzed with FlowJo software.

2.13 RNA-sequencing and bioinformatics analysis

Total RNA was extracted from harvested tumor and lymph node tissues using the AG RNAex Pro Reagent (Accurate Biotechnology, China). Poly(A) mRNA was purified using Oligo(dT) magnetic beads and randomly fragmented. Synthesis of cDNA, adapter ligation, and library construction were performed prior to sequencing on an Illumina NovaSeq 6000 platform (OE Biotech, Inc., Shanghai, China) with 150 bp paired-end reads.

The raw reads were processed using fastp (0.20.1) for quality control and aligned to the mouse reference genome (NCBI_GRCm39) using HISAT2 (2.1.0). Gene quantification was performed using htseq-count (0.11.2). Differential expression analysis was conducted using DESeq2 (1.22.2), with thresholds set at $|\log_2 FC| > 1$ and $p < 0.05$. Functional enrichment analyses, including Gene Ontology (GO) and Kyoto Encyclopedia of Genes and Genomes (KEGG), were performed using the OECloud tools (https://cloud.oebiotech.com/task/).

2.14 Histological and immunofluorescence analysis

Excised tumor tissues were fixed in 4% paraformaldehyde, paraffin-embedded, and sectioned for evaluation. Cell proliferation and apoptosis were assessed via TUNEL staining, respectively. For multiplex immunofluorescence, tumor sections underwent deparaffinization, antigen retrieval, and quenching of endogenous peroxidase. Sections were incubated with primary antibodies including rabbit anti-mouse CD4 (1:200, Abcam, ab288724), CD8α (1:200, Servicebio, GB15068), CD86 (1:200, CST, 19589), and CD206 (1:1500, Abcam, ab64693).

Signal amplification was achieved using Tyramide Signal Amplification (TSA) with Cy3 or Alexa Fluor 488 fluorophores. For multiplex visualization, sequential rounds of staining and antibody stripping via microwave treatment were performed. Nuclei were counterstained with DAPI, and slides were mounted with ProLong Diamond Antifade Mountant (Thermo Fisher, P36961). Images were captured using a Zeiss LSM 880 confocal microscope and quantitatively analyzed via ImageJ software to assess the immune microenvironment landscape.

2.15 Western blot analysis for cGAS-STING pathway

Tumor tissues were lysed in RIPA buffer supplemented with protease and phosphatase inhibitors (Roche/Servicebio). Total protein concentrations were determined, and 40 μg total protein was separated via SDS-PAGE and transferred to 0.45 μm PVDF membranes (Millipore). Membranes were blocked with 5% non-fat milk and incubated overnight at 4°C with the following primary antibodies: cGAS (1:1000, ABclonal, A8335), STING (1:50000, Proteintech, 19851-1-AP), P-STING (1:1000, ABclonal, AP1369), P-TBK1 (1:10000, ABclonal, AP1026), P-IRF3 (1:10000, ABclonal, AP0857), IFN-β (1:2000, ABclonal, A25818), and p-STAT1 (1:10000, Proteintech, 82016-1-RR). GAPDH (1:10000, Proteintech, 60004-1-Ig) was used as a loading control. After incubation with HRP-conjugated secondary antibodies (1:20,000, Seracare; anti-rabbit 5220 – 0336 or anti-mouse 5220 – 0341) for 1 h, protein bands were visualized using an ECL chemiluminescence kit and a SCG-W3000plus imaging system. Band densities were quantified using ImageJ software.

2.16 Statistical Analysis

All quantitative data are presented as mean ± standard deviation (SD). Statistical significance between two groups was determined using unpaired two-tailed Student’s t-tests, and comparisons among multiple groups were performed using one-way ANOVA followed by Tukey’s post-hoc test. A p-value < 0.05 was considered statistically significant. GraphPad Prism 9.0 was used for statistical analysis.

3. Results

3.1 Structural characterization of GP and formulation optimization of COS@GP

The primary structure of GP was first validated to ensure the reproducibility of the nanoassembly. PMP-HPLC analysis revealed that GP is a neutral-dominant heteropolysaccharide, primarily composed of glucose (96.4%), with minor amounts of uronic acids and other neutral sugars (< 4% in total) (Fig. S1, Table S1). GPC analysis showed a weight-average molecular weight (M_w) of 23.3 kDa with a polydispersity index (PDI) of 1.51 (Fig. S2, Table S2).

Subsequently, COS@GP were fabricated via a one-pot electrostatic assembly process. To systematically identify the optimal formulation, a Plackett-Burman design (PBD) was employed to evaluate three independent variables: the concentrations of COS, GP, and TPP (Table S3). Under the optimized mass

ratio of 4:3:0.5 (COS:GP:TPP, w/w/w), the resulting COS@GP exhibited a hydrodynamic diameter of 229 ± 18.6 nm, a low PDI of 0.25 ± 0.01, and a moderately positive zeta potential of 13.1 ± 0.9 mV (Fig. 1b-c).

Morphological characterization via SEM and TEM consistently revealed discrete, well-defined spherical nanostructures (Fig. 1d-e). The observed TEM diameter was slightly smaller than the DLS result, a phenomenon attributed to the dehydration and shrinkage of the polysaccharide shell during sample preparation. Furthermore, the COS@GP demonstrated robust storage stability at 4°C for one week and maintained their physicochemical integrity after lyophilization and reconstitution (Table S4).

3.2 Spectroscopic characterization of COS@GP self-assembly

We employed a 2D FTIR@Raman integrated analytical strategy to decouple the driving forces and conformational transitions involved in the formation of COS@GP. FT-IR spectra (Fig. 1f) confirmed that the assembly was driven by ionic complexation and hydrogen bonding. In contrast to the physical mixture, COS@GP exhibited a pronounced attenuation of the O–H/N–H stretching (3380 cm^{-1}) and glycosidic vibrations (1070 and 1150 cm^{-1}), indicating robust electrostatic interactions between COS amines and GP carboxyl groups. Specifically, the disappearance of the C–OH bending band at 1410 cm^{-1} suggested the successful sequestration of GP chains within a densely cross-linked core.

Raman spectroscopy further revealed a transition from disordered chains to a more organized backbone. The C–H stretching near 2900 cm^{-1} exhibited distinct splitting, and the sharpening of C–C vibration peaks at 1063 cm^{-1} suggested an adjustment of the carbon chain environment (Fig. 1g). Notably, the emergence of a skeletal vibration peak near 200 cm^{-1} (absent in precursors) provided direct evidence of increased structural order and chain orientation within the nanoconfined space.

To clarify the interaction hierarchy, 2D correlation spectroscopy (Fig. 1h-i, Table 1) was applied. Synchronous maps showed positive cross-peaks between 895 cm^{-1} (β-pyranose ring) and 980 cm^{-1} (COS C–N/C–O), indicating a cooperative association driven by multi-site hydrogen bonding. Conversely, the negative cross-peaks between 1030 and 1079 cm^{-1} reflected a significant conformational rearrangement of GP glycosidic linkages. Asynchronous analysis established the sequence of events: intensity variations at 980 cm^{-1} (COS) preceded those at 1030 cm^{-1} (GP backbone). This confirms that the assembly is initiated by the active anchoring of COS onto GP, which subsequently induces a secondary, coordinated adjustment of the GP chain conformation to achieve a stable nanostructure.

Table 1
Signs of cross-peaks in synchronous and asynchronous 2D FTIR correlation spectra of COS@GP. A positive (+) sign indicates that the transition intensities of the two peaks change in the same direction (both increasing or decreasing), while a negative (-) sign indicates they change in opposite directions.

Peak(cm^{-1})	Band assignment	Sign*					
		895	**980**	**1030**	**1079**	**1140**	**1180**
895		+	+ (+)	− (−)	− (−)	+ (−)	+ (−)
980			+	− (−)	− (−)	+ (−)	+ (−)
1030				+	− (+)	+ (−)	+ (+)
1079					+	+ (+)	+ (+)
1140						+	+ (+)
1180							+

3.3 Gastrointestinal Stability and Release of COS@GP

The oral delivery efficiency of COS@GP depends on their stability in the gastrointestinal environment and their ability to release GP in the intestinal phase. As illustrated in Fig. 1j, COS@GP maintained stable particle size in simulated gastric fluid (SGF, pH 1.2), remaining within the range of 240–280 nm during the 2 h incubation. This result indicates that the COS@GP nanostructure remains stable under acidic conditions. The stability is likely associated with the ionic network formed by COS and GP and further stabilized by TPP cross-linking. After transfer to simulated intestinal fluid (SIF, pH 6.8), a moderate increase in particle size and slight changes in PDI were observed. These results suggest partial swelling and structural relaxation of the nanoparticles in the intestinal environment.

To quantify the release of GP, the cumulative release profile was evaluated by measuring the reducing sugar content (Fig. 1k). In the SGF phase, COS@GP showed minimal release, with the cumulative release remaining below 12%, indicating that the nanoparticle structure effectively limited premature GP release under acidic conditions. After transition to the SIF phase, the system exhibited a gradual increase in release, reaching approximately 55% over 8 h. The increase in reducing sugar content reflects the progressive dissociation of the COS@GP assembly and the subsequent release of GP. In contrast, free GP showed unstable concentration changes during the digestion process, likely due to uncontrolled degradation. These results indicate that the COS@GP structure provides improved stability in the gastric environment while enabling sustained GP release under intestinal conditions.

To evaluate the effect of COS@GP on intestinal homeostasis, transcriptomic profiling was performed in healthy mice. Principal component analysis (PCA) and Pearson correlation analysis demonstrated high consistency among samples, with a modest separation between groups (Fig. S3a, b). COS@GP induced 116 differentially expressed genes (DEGs), including 80 upregulated and 36 downregulated genes.

Among these, several genes associated with mucosal defense, such as Defa25 and Saa1, were upregulated, whereas genes related to lipid metabolism, including Fabp6 and Slc25a48, were downregulated (Fig. S3c–f). Gene set enrichment analysis (GSEA) further indicated enrichment of innate immune response–related pathways in intestinal tissues without a significant increase in pro-inflammatory cytokine genes such as Il6 (Fig. S3g–i). These findings suggest that COS@GP modulates intestinal immune-related transcriptional programs while maintaining mucosal immune homeostasis.

3.4 Cellular uptake and biocompatibility of COS@GP

The safety profile of COS@GP was evaluated across multiple cell lines relevant to systemic and mucosal immunity, including 4T1, DC2.4, RAW 264.7, and Caco-2 cells. As shown in Fig. S4, both free GP and COS@GP exhibited minimal cytotoxicity even at high concentrations, with cell viability remaining above 90% in all tested groups. These results indicate that the COS@GP formulation shows good biocompatibility for subsequent cellular studies.

To investigate cellular internalization, three formulations were compared: free GP, the physical mixture (COS/GP), and COS@GP. CLSM was first employed to visualize the uptake in 4T1 and DC2.4 cells (Fig. 2a, d). In both cell types, COS@GP treatment resulted in stronger intracellular fluorescence signals compared with GP and COS/GP. Clear co-localization of FITC-GP (green) and RhB-COS (red) was observed within the cytoplasm, indicating that COS and GP were internalized as a co-assembled structure. A similar pattern was observed in Caco-2 cells (Fig. S5a), suggesting that the nanoparticle structure promotes cellular uptake.

To quantitatively assess internalization efficiency, flow cytometry analysis was performed. In DC2.4 cells, COS@GP significantly increased both the percentage of fluorescent cells and the mean fluorescence intensity (MFI) compared with GP and COS/GP (Fig. 2b, c). A consistent trend was observed in 4T1 cells, where COS@GP also produced the highest MFI among all groups (Fig. 2e, f). Similar results were obtained in Caco-2 cells (Fig. S5b, c), confirming that the self-assembled COS@GP structure enhances cellular uptake across multiple cell types.

3.5 M-cell-mediated transcytosis of COS@GP

To quantify nanocarrier transport in subsequent experiments, fluorescently labeled polymers were prepared. Based on the standard curves of FITC and RhB (Fig. S6, S7), the labeling efficiency was determined to be 0.02% (w/w) for FITC-GP and 0.63% (w/w) for RhB-COS. These values were used to calculate the concentrations of labeled nanocarriers in subsequent in vitro and *ex vivo* experiments.

An *in vitro* M-cell co-culture model was established to mimic the intestinal FAE (Fig. 2g). The model involved the systematic differentiation of Caco-2 and HT-29 cells, followed by the addition of Raji B cells to induce M-cell differentiation over a 21-day culture period. Successful M-cell formation was confirmed by TEM imaging, which showed the typical reduction of dense microvilli and the presence of sparse microfold structures on the apical surface (Fig. 2h). The transcytosis of GP and COS@GP was then evaluated using the M-cell model over a 4 h period (Fig. 2i). Compared with free GP, COS@GP exhibited a

significantly higher cumulative transport percentage across the M-cell layer. These results indicate that the COS@GP nanostructure enhances transport across the M-cell-associated intestinal barrier.

3.6 SPIP analysis of intestinal permeability

To validate mucosal permeability under physiological conditions, the SPIP model was employed, focusing on the jejunum as the target region for Peyer's patches.

As summarized in Table 2, both the absorption rate constant ($K_{a)}$ and effective permeability coefficient (P_{eff}) revealed distinct differences among formulations. Compared to free GP (0.0988 ± 0.0065x10^{-2}/min; P_{eff}=0.0432 ± 0.0009×10^{-3} cm/min), COS@GP exhibited a significant increase in both parameters, outperforming both the GP and COS/GP. Specifically, the P_{eff} of COS@GP was increased by 113.8% compared to that of COS/GP.

Table 2

K_a and P_{eff} of GP formulations in jejunum ($x \pm s, n = 6$).

Formulation	Concentration (mg/mL)	K_a (x10^{-2} /min)	P_{eff} (x10^{-3} cm/min)
GP	0.5	0.098 ± 0.0064	0.032 ± 0.0004
	1.0	0.0988 ± 0.0065	0.0432 ± 0.0009
COS	0.5	2.3628 ± 0.3096	2.4975 ± 0.3599
	1.0	2.7018 ± 0.2422	2.4815 ± 0.2633
COS/GP	0.5	0.8909 ± 0.3886$^{*\#}$	1.2931 ± 0.1313$^{*\#}$
	1.0	1.1093 ± 0.1113$^{*\#}$	1.4643 ± 0.1164$^{*\#}$
COS@GP	0.5	3.0925 ± 0.3754$^{*\#\triangle}$	3.3806 ± 0.3796$^{*\#\triangle}$
	1.0	3.0100 ± 0.2831$^{*\#\triangle}$	3.1302 ± 0.1932$^{*\#\triangle}$
Note: *P, #P, ΔP < 0.0001 vs. GP, COS, and COS/GP, respectively.			

These results demonstrate that the COS@GP significantly enhances the transport of GP across the intestinal barrier. This improved permeability in the jejunum is consistent with the M-cell transcytosis data, confirming that COS@GP more than doubled the transport efficiency compared to the physical mixture, thereby facilitating the delivery of GP to the underlying lymphoid tissues for immune uptake.

3.7 *In vivo* biodistribution and Peyer's patches targeting

To elucidate the systemic distribution kinetics and Peyer's patches targeting characteristics of the nanocarriers, real-time *in vivo* fluorescence imaging was performed over a 12-hour period. Following oral

administration, the free FITC-GP group exhibited rapid systemic clearance, with fluorescence signals quickly and predominantly accumulating in the urinary tract region, indicating that the free polysaccharide was mainly excreted in its prototype form via urine (Fig. S8). In contrast, the COS/GP physical mixture group showed only marginal abdominal fluorescence at the 2 h and 4 h time points. However, the COS@GP group maintained robust and stable fluorescence signals throughout the gastrointestinal tract for up to 12 h. This significantly prolonged intestinal retention confirms that the COS-decorated nanostructure imparts superior mucoadhesive properties to the formulation.

Ex vivo tissue imaging further validated these distribution trends. At 2 h and 4 h post-administration, the intestinal accumulation in the COS@GP group was significantly higher than that in the free GP and physical mixture groups (Fig. 3a). Beyond the gastrointestinal tract, fluorescence signals were also detectable in the liver, kidneys, lungs, and notably, the tumor-draining lymph nodes (TDLN), suggesting systemic dissemination following mucosal penetration (Fig. 3b). A direct *ex vivo* comparison at the 2 h mark revealed that the nanocarriers exhibited enhanced permeability across the entire intestinal view compared to the physical mixture, with a distinct trend of COS signal accumulation in the Peyer's patch regions (Fig. 3c).

Subsequent localization studies focusing on Peyer's patches, the primary gateways for mucosal immunity, showed that FITC-GP signals in the COS@GP group were specifically enriched within the lymphoid follicles (Fig. 3d). Histological quantification confirmed a marked increase in GP internalization compared to the physical mixture (Fig. 3e). Furthermore, the high Manders' colocalization coefficient in the COS@GP group (Fig. 3f) strongly indicated that the nanocarriers reached the lymphoid tissues as intact assemblies rather than dissociated fragments. These *in vivo* findings are highly consistent with the M-cell transcytosis and SPIP permeability data, collectively proving that COS@GP effectively leverages the M-cell-mediated immune-sampling pathway to achieve targeted delivery of polysaccharides to gut-associated lymphoid tissues.

3.8 Synergistic Antitumor Efficacy and Lymphatic-Dependent Immune Activation

The therapeutic potential of COS@GP was evaluated using a 4T1 subcutaneous tumor model (Fig. 4a-e). While oral administration of COS@GP alone showed limited efficacy with a tumor inhibition rate (TIR) of only 20.3%, its combination with radiotherapy (RT+COS@GP) resulted in the most robust tumor suppression, achieving a significant TIR of 71%. This was 1.78-fold higher than that of the free polysaccharide group (RT+GP, 39.9%), demonstrating that the nano-assembly significantly amplifies the radio-sensitizing effect of GP.

To confirm that the superior efficacy of COS@GP stems from its specialized intestinal lymphatic entry, the lymphatic-homing inhibitor FTY720 was employed. FTY720 downregulates $S1P_1$ receptors, thereby sequestering activated lymphocytes within lymphoid tissues and blocking their systemic circulation. Upon FTY720 treatment, the TIR of the RT+COS@GP group dropped from 71% to 56.6%. This partial reversal of therapeutic benefit provides direct evidence that the antitumor immune response of COS@GP is highly dependent on the gut-associated lymphatic transport pathway.

Histological analysis further supported these observations (Fig. 4i). The RT+COS@GP group exhibited reduced markedly increased TUNEL-positive apoptotic signals compared to RT+GP, indicating enhanced tumor cell death and suppressed proliferation. H&E staining revealed extensive structural disruption within tumor tissues following combination treatment.

Beyond tumor reduction, COS@GP effectively mitigated RT-induced systemic toxicity (Fig. S9). While the RT group exhibited weight loss due to radiation-induced damage, the RT+COS@GP group showed accelerated weight recovery, indicating a "sensitization without added toxicity" profile. Serum cytokine profiling via ELISA (Fig. 4f-h) further revealed that RT+COS@GP shifted the systemic immune environment toward a pro-inflammatory Th1 phenotype. Specifically, the levels of IFN-γ and TNF-α were significantly elevated in the RT+COS@GP group compared to the RT+GP cohort ($P < 0.01$). This potentiation was significantly blunted by FTY720 ($P < 0.05$), confirming that activated immune cells must migrate from the lymphatic system to the tumor site to exert their effects.

Interestingly, while RT triggered a spike in IL-6—a multi-functional cytokine often associated with RT-induced acute inflammation—the addition of COS@GP helped modulate this response, suggesting a role in maintaining immune homeostasis. In summary, these results demonstrate that COS@GP acts as a potent mucosal adjuvant. By leveraging its nano-scale advantage for efficient Peyer’s patch uptake, it systematically primes the immune system to synergize with radiotherapy, driving a lymphatic-dependent systemic antitumor response.

3.9 Enhancement of DC Maturation and Effector T Cell Infiltration

Flow cytometric analysis was performed to evaluate the effect of COS@GP on DC activation in TDLN. As shown in Figure 5a, b and Figure S10, radiotherapy alone significantly reduced the proportion of mature DC ($CD11c^+CD80^+CD86^+$) compared with the model group, indicating that irradiation impaired antigen-presenting activity within TDLN. In contrast, the RT + COS@GP group exhibited a marked increase in the frequency of mature DC, representing the highest level among all treatment groups. Oral administration of COS@GP alone also moderately increased DC maturation compared with the model group, suggesting that COS@GP possesses intrinsic immunostimulatory activity within the lymphatic immune compartment. Notably, blocking lymphocyte trafficking with FTY720 did not significantly alter the maturation status of DC in TDLN, indicating that COS@GP-mediated DC activation occurs upstream of lymphocyte circulation.

Consistent with the enhanced DC maturation observed in TDLN, a pronounced increase in effector T-cell infiltration was detected in tumor tissues. Flow cytometry revealed that the RT + COS@GP group displayed the highest proportions of tumor-infiltrating $CD8^+$ cytotoxic T cells and $CD4^+$ helper T cells among all groups (Fig. 5c, d and Fig. S11). In contrast, radiotherapy alone resulted in a reduction of tumor-infiltrating T cells relative to the model group. Importantly, the accumulation of tumor-infiltrating T cells was markedly attenuated in the RT + COS@GP + FTY720 group, indicating that lymphatic trafficking plays a critical role in the systemic immune activation induced by oral COS@GP.

Multiplex immunofluorescence staining of tumor sections further confirmed these findings. As shown in Figure 6a-b, abundant $CD4^+$ and $CD8^+$ T cells were observed within tumors from the RT + COS@GP group, whereas substantially fewer T cells were detected in tumors from the RT and model groups. These observations demonstrate that COS@GP treatment promotes the recruitment and accumulation of effector T cells within the tumor microenvironment.

In addition to adaptive immune activation, COS@GP also altered macrophage composition within the tumor microenvironment. Flow cytometric analysis showed that radiotherapy alone increased the proportion of $CD206^+$ M2-like macrophages while reducing $CD86^+$ M1-like macrophages (Fig. 5e-g and Fig. S12). In contrast, the RT + COS@GP treatment significantly increased $CD86^+$ macrophages and decreased $CD206^+$ macrophages, resulting in an elevated M1/M2 ratio. This shift in macrophage phenotype was consistent with the enhanced antitumor immune observed in the RT + COS@GP group.

Immunofluorescence staining further supported these results. As shown in Figure 6c-d, tumors from the RT + COS@GP group exhibited increased $CD86^+$ macrophages and reduced $CD206^+$ macrophages compared with the RT group. Spatially, $CD86^+$ macrophages were frequently observed at the tumor–stroma interface, suggesting localized innate immune activation within the tumor microenvironment.

3.10 Activation of the cGAS-STING Pathway in Tumors

To further investigate the molecular mechanism underlying the enhanced antitumor immune response induced by COS@GP, the activation of the cGAS-STING signaling pathway in tumor tissues was examined by western blot. As shown in Figure 7a, radiotherapy alone slightly increased the expression of cGAS and downstream signaling molecules compared with the model group. Notably, the combination of COS@GP with radiotherapy markedly enhanced the activation of the cGAS-STING signaling cascade.

Quantitative analysis further confirmed that the RT + COS@GP group exhibited higher levels of phosphorylated STING, TBK1, and IRF3 compared with the RT group (Fig. 7b–g). In addition, the expression of IFN-β, a key downstream effector of cGAS–STING signaling, was significantly elevated in the RT + COS@GP group. These results indicate that COS@GP enhances radiotherapy-induced activation of the cGAS–STING pathway, thereby promoting innate immune signaling within the tumor microenvironment.

3.11 Transcriptomic profiling reveals immune pathway remodeling

To further elucidate the molecular mechanisms underlying the therapeutic effect of COS@GP combined with radiotherapy, transcriptomic profiling was performed on tumor tissues. Principal component analysis (PCA) demonstrated a clear separation between the RT and RT+COS@GP groups, indicating distinct transcriptional landscapes between treatments (Fig. S13a). Differential expression analysis identified numerous genes significantly altered by the combined treatment, as visualized in the volcano plot (Fig. 8a).

Functional enrichment analysis revealed that these differentially expressed genes were primarily associated with immune-related biological processes. KEGG pathway analysis highlighted multiple immune-associated pathways (Fig. 8b), while Gene Ontology (GO) analysis further indicated enrichment in immune regulation and immune cell-related processes (Fig. 8c and Fig. S13b-d).

Gene set enrichment analysis (GSEA) further revealed significant enrichment of immune-associated pathways, including hematopoietic cell lineage, antigen processing and presentation, and Th1 and Th2 cell differentiation (Fig. 8d-f). Collectively, these transcriptomic findings suggest that COS@GP in combination with radiotherapy reshape the tumor immune transcriptional landscape, supporting enhanced immune modulation within the tumor microenvironment.

4. Discussion

Oral delivery of polysaccharides has long been limited by the assumption that these macromolecules lack direct immunological accessibility and primarily act through indirect mechanisms such as microbiota modulation [33,34]. In contrast, this study demonstrates that polysaccharide function can be fundamentally redefined by structural organization, enabling a pathway-defined immune entry via Peyer's patches [35,36]. Rather than undergoing passive gastrointestinal processing, the nano-assembled COS@GP system redirects GP toward active mucosal immune engagement, establishing a functional link between oral administration and systemic immune activation.

This shift is enabled by structure-guided assembly. While GP alone suffers from instability and uncertain biological fate, its integration with COS produces a functionally organized architecture [37]. The cationic COS framework not only stabilizes GP through electrostatic condensation but also enhances mucosal retention and facilitates interaction with follicle-associated epithelium [38]. Beyond structural support, COS contributes to innate immune priming, potentially cooperating with downstream pathways such as cGAS-STING signaling [39]. Thus, COS@GP operates not as a conventional carrier system but as an integrated immunologically active assembly in which structure and function are intrinsically coupled.

Spectroscopic analysis further supports that COS@GP forms through charge-driven organization rather than random aggregation, resulting in nanoconfinement that preserves GP integrity during gastrointestinal transit.

Functionally, this structural design translates into a defined immune entry pathway. The particle size of COS@GP (~240 nm) aligns with the optimal range for M cell–mediated sampling, enabling direct access to Peyer's patches [40]. Combined with its stability and enhanced transcytosis, COS@GP bypasses nonspecific epithelial absorption and achieves targeted delivery to intestinal immune inductive sites [41]. This establishes a pathway-defined mechanism in which structural organization governs immune accessibility [42].

The role of intestinal lymphatic transport was further supported by FTY720 inhibition, which partially attenuated the therapeutic effect. This indicates that Peyer's patch–mediated immune activation

constitutes a major, but not exclusive, pathway. Additional contributions likely arise from intrinsic COS immunostimulation and radiotherapy-induced tumor signaling, supporting a cooperative model of systemic immune activation.

In this context, COS@GP functions as a mucosal immune primer rather than an independent cytotoxic agent. Radiotherapy provides downstream amplification through immunogenic cell death and DNA sensing pathways. The convergence of mucosal priming and tumor-derived danger signaling, potentially involving the cGAS-STING axis, underlies the enhanced systemic antitumor response.

Transcriptomic analysis further supports this framework, showing enrichment of antigen presentation, hematopoietic lineage, and Th1/Th2 differentiation pathways. These findings are consistent with the observed activation of dendritic cells, T cells, and macrophage polarization, reinforcing that COS@GP reshapes the tumor immune microenvironment toward an immunologically responsive state.

Despite these findings, several questions remain. The relative contribution of Peyer's patches versus alternative intestinal uptake pathways requires further clarification, and the precise immune signaling events within GALT remain to be resolved. In addition, the link between mucosal immune priming and systemic cGAS–STING activation warrants further investigation.

5. Conclusions

In this study, we developed a structure-guided polysaccharide nanoassembly (COS@GP) that enables pathway-defined oral immune entry through Peyer's patches. The electrostatic self-assembly between chitosan oligosaccharide and ginseng polysaccharide generated stable nanostructures with favorable gastrointestinal stability, enhanced intestinal permeability, and efficient M-cell–mediated transcytosis, leading to targeted accumulation in gut-associated lymphoid tissues. Functionally, oral administration of COS@GP significantly enhanced the therapeutic efficacy of radiotherapy by promoting dendritic cell maturation, increasing effector T-cell infiltration, and repolarizing tumor-associated macrophages. Mechanistically, these immune responses were associated with enhanced activation of cGAS–STING-related signaling and transcriptomic reprogramming of immune pathways within the tumor microenvironment.

Overall, this work demonstrates that supramolecular organization can determine the immunological fate of orally administered polysaccharides. By converting freely dispersed polysaccharides into immune-accessible nanostructures, COS@GP establishes a practical strategy for oral radio-immunotherapy and provides a conceptual framework for the rational design of polysaccharide-based immunotherapeutic systems.

Abbreviations

H
heart,Li,liver

Sp
spleen
Lu
lung
K
kidney
TDLN
tumor-draining lymph nodes
T
tumor.

Declarations

CRediT authorship contribution statement

Zheming Hu: Formal analysis, Investigation, Validation, Visualization, Writing-review & editing. **Qin Zhang:** Methodology, Data curation, Visualization, Writing-original draft. **Haojie Wang:** Methodology, Data curation, Visualization. **Wulong Wen: Methodology,** Visualization. **Lingfan Fan:** Methodology, Visualization. **Jinxuan Yang:** Visualization. **Shuhui Geng:** Visualization. **Lan Qin:** Visualization. **Fengyi Ma:** Visualization. **Yang Lu:** Conceptualization, Data curation, Supervision.

Declaration of competing interest

The authors declare that they have no competing interests.

Data Availability

The data that support the findings of this study are available from the corresponding author upon reasonable request.

Funding

This work was supported by the Beijing Nova Program (Grant No. 20240484544), the China Institute of Atomic Energy (Grant No. CNNNCWZ-2023002), and the State Administration of Traditional Chinese Medicine of the People's Republic of China (Grant No. zyyzdxk-2023272).

Ethics approval

All animal experimental protocols were reviewed and approved by the Institutional Animal Care and Use Committee (IACUC) of Beijing University of Chinese Medicine (Approval No. BUCM20250724-002 and BUCM20250814-003). All procedures were performed in strict accordance with the Guide for the Care and Use of Laboratory Animals.

Consent to Publish

Consent to Publish declaration: not applicable.

References

1. S. Billan, O. Kaidar-Person, Z. Gil, Treatment after progression in the era of immunotherapy, The Lancet Oncology 21 (2020) e463–e476. https://doi.org/10.1016/S1470-2045(20)30328-4.
2. Spotlight on cancer immunotherapies, Nat Biotechnol 43 (2025) 453–454. https://doi.org/10.1038/s41587-025-02645-5.
3. S.N. Khleif, S. Gupta, Cancer vaccines as enablers of immunotherapy, Nat Immunol 26 (2025) 1877–1889. https://doi.org/10.1038/s41590-025-02308-2.
4. B.J. Kim, N.S. Abdelfattah, A. Hostetler, D.J. Irvine, Progress in cancer vaccines enabled by nanotechnology, Nat. Nanotechnol. 20 (2025) 1558–1572. https://doi.org/10.1038/s41565-025-02021-z.
5. Y. Tan, R. Xue, Y. Pan, Z. He, X. Hu, Y. Li, K. Li, X. Zhang, X. Bian, B. Wang, Cancer cachexia: molecular basis and therapeutic advances, Sig Transduct Target Ther 11 (2026) 16. https://doi.org/10.1038/s41392-025-02331-7.
6. A.P. Singh, A. Biswas, A. Shukla, P. Maiti, Targeted therapy in chronic diseases using nanomaterial-based drug delivery vehicles, Sig Transduct Target Ther 4 (2019) 33. https://doi.org/10.1038/s41392-019-0068-3.
7. V.F. Gomerdinger, N. Nabar, P.T. Hammond, Advancing engineering design strategies for targeted cancer nanomedicine, Nat Rev Cancer 25 (2025) 657–683. https://doi.org/10.1038/s41568-025-00847-2.
8. P. Tso, J. Bernier-Latmani, T.V. Petrova, M. Liu, Transport functions of intestinal lymphatic vessels, Nat Rev Gastroenterol Hepatol 22 (2025) 127–145. https://doi.org/10.1038/s41575-024-00996-z.
9. T.L.B. Hoelting, T. Park, C.C. Brown, Antigen-presenting cells as arbiters of mucosal tolerance and immunity, Nat Immunol 26 (2025) 1890–1902. https://doi.org/10.1038/s41590-025-02320-6.
10. V. Cerovic, O. Pabst, A.M. Mowat, The renaissance of oral tolerance: merging tradition and new insights, Nat Rev Immunol 25 (2025) 42–56. https://doi.org/10.1038/s41577-024-01077-7.
11. X. Zhou, Y. Wu, Z. Zhu, C. Lu, C. Zhang, L. Zeng, F. Xie, L. Zhang, F. Zhou, Mucosal immune response in biology, disease prevention and treatment, Sig Transduct Target Ther 10 (2025) 7. https://doi.org/10.1038/s41392-024-02043-4.
12. F. Zhao, C. Yin, M. Cao, Y. Qian, L. Zhang, Y. Tian, X. Zhong, X. Fang, A. Tao, The potential, challenges, and prospects of Panax quinquefolium L. polysaccharides as future multipurpose biomacromolecules, Int J Biol Macromol 304 (2025) 140769. https://doi.org/10.1016/j.ijbiomac.2025.140769.
13. B. Li, J. Cui, T. Xu, Y. Xu, M. Long, J. Li, M. Liu, T. Yang, Y. Du, Q. Xu, Advances in the preparation, characterization, and biological functions of chitosan oligosaccharide derivatives: A review, Carbohydr Polym 332 (2024) 121914. https://doi.org/10.1016/j.carbpol.2024.121914.

14. I. Mukhopadhya, P. Louis, Gut microbiota-derived short-chain fatty acids and their role in human health and disease, Nat Rev Microbiol 23 (2025) 635–651. https://doi.org/10.1038/s41579-025-01183-w.
15. J. Nam, A. Kim, K. Kim, J.H. Moon, J. Baig, M. Phoo, J.J. Moon, S. Son, Engineered polysaccharides for controlling innate and adaptive immune responses, Nat Rev Bioeng 2 (2024) 733–751. https://doi.org/10.1038/s44222-024-00193-2.
16. J.N. Chu, G. Traverso, Foundations of gastrointestinal-based drug delivery and future developments, Nat Rev Gastroenterol Hepatol 19 (2022) 219–238. https://doi.org/10.1038/s41575-021-00539-w.
17. T.H. Baryakova, B.H. Pogostin, R. Langer, K.J. McHugh, Overcoming barriers to patient adherence: the case for developing innovative drug delivery systems, Nat Rev Drug Discov 22 (2023) 387–409. https://doi.org/10.1038/s41573-023-00670-0.
18. M. Rawas-Qalaji, H.E. Thu, Z. Hussain, Oromucosal delivery of macromolecules: Challenges and recent developments to improve bioavailability, Journal of Controlled Release 352 (2022) 726–746. https://doi.org/10.1016/j.jconrel.2022.10.059.
19. S. Lian, W. Yang, Y. Zeng, R. Tang, K. Wang, Targeted nano-drug delivery systems for tumor immunotherapy, Journal of Pharmaceutical Analysis (2025) 101408. https://doi.org/10.1016/j.jpha.2025.101408.
20. M.-M. Han, Y.-K. Fan, Y. Zhang, Z.-Q. Dong, Advances in herbal polysaccharides-based nano-drug delivery systems for cancer immunotherapy, J Drug Target 32 (2024) 311–324. https://doi.org/10.1080/1061186X.2024.2309661.
21. P.A.R. Fernandes, M.A. Coimbra, The antioxidant activity of polysaccharides: A structure-function relationship overview, Carbohydr Polym 314 (2023) 120965. https://doi.org/10.1016/j.carbpol.2023.120965.
22. S. Guo, Y. Yao, Y. Tang, Z. Xin, D. Wu, C. Ni, J. Huang, Q. Wei, T. Zhang, Radiation-induced tumor immune microenvironments and potential targets for combination therapy, Sig Transduct Target Ther 8 (2023) 205. https://doi.org/10.1038/s41392-023-01462-z.
23. Y. Lan, M. Moustafa, M. Knoll, C. Xu, J. Furkel, A. Lazorchak, T.-L. Yeung, S.-M. Hasheminasab, M.H. Jenkins, S. Meister, H. Yu, J. Schlegel, B. Marelli, Z. Tang, G. Qin, C. Klein, J. Qi, C. Zhou, G. Locke, D. Krunic, M.G. Derner, C. Schwager, R.E. Fontana, K. Kriegsmann, F. Jiang, K. Rein, M. Kriegsmann, J. Debus, K.-M. Lo, A. Abdollahi, Simultaneous targeting of TGF-β/PD-L1 synergizes with radiotherapy by reprogramming the tumor microenvironment to overcome immune evasion, Cancer Cell 39 (2021) 1388-1403.e10. https://doi.org/10.1016/j.ccell.2021.08.008.
24. Y. Yan, X. Tan, B. Song, M. Yi, Q. Chu, K. Wu, Breaking barriers: The cGAS-STING pathway as a novel frontier in cancer immunotherapy, Cancer Communications 45 (2025) 1513–1546. https://doi.org/10.1002/cac2.70067.
25. M. Shen, X. Jiang, Q. Peng, L. Oyang, Z. Ren, J. Wang, M. Peng, Y. Zhou, X. Deng, Q. Liao, The cGAS–STING pathway in cancer immunity: mechanisms, challenges, and therapeutic implications, J Hematol Oncol 18 (2025) 40. https://doi.org/10.1186/s13045-025-01691-5.

26. C. Lu, W. Wang, Y.-X. Fu, Opportunities and challenges of targeting cGAS–STING in cancer, Nat Rev Cancer (2026) 1–17. https://doi.org/10.1038/s41568-025-00894-9.
27. Z. Zheng, X. Pan, L. Luo, Q. Zhang, X. Huang, Y. Liu, K. Wang, Y. Zhang, Advances in oral absorption of polysaccharides: Mechanism, affecting factors, and improvement strategies, Carbohydr Polym 282 (2022) 119110. https://doi.org/10.1016/j.carbpol.2022.119110.
28. Z. Zheng, X. Pan, J. Xu, Z. Wu, Y. Zhang, K. Wang, Advances in tracking of polysaccharides in vivo: Labeling strategies, potential factors and applications based on pharmacokinetic characteristics, Int J Biol Macromol 163 (2020) 1403–1420. https://doi.org/10.1016/j.ijbiomac.2020.07.210.
29. Gut microbiota-mediated immunomodulation underlies the anti-tumor effects of a novel ginseng polysaccharide, Carbohydrate Polymers 370 (2025) 124458. https://doi.org/10.1016/j.carbpol.2025.124458.
30. A. García-Rodríguez, L. Vila, C. Cortés, A. Hernández, R. Marcos, Exploring the usefulness of the complex *in vitro* intestinal epithelial model Caco-2/HT29/Raji-B in nanotoxicology, Food and Chemical Toxicology 113 (2018) 162–170. https://doi.org/10.1016/j.fct.2018.01.042.
31. K.S. Italiya, A.K. Singh, D. Chitkara, A. Mittal, Nanoparticulate tablet dosage form of lisofylline-linoleic acid conjugate for type 1 diabetes: in situ single-pass intestinal perfusion (SPIP) studies and pharmacokinetics in rat, AAPS PharmSciTech 22 (2021) 114. https://doi.org/10.1208/s12249-021-01980-5.
32. W. Li, X. Yang, M. Wang, Z. Hu, S. Chen, X. Sui, D. Chen, X. Niu, J. Liu, Y. Xiao, X. Zhou, G. Chen, Y. Gao, Development of a Cascade-Targeting Oral Vaccine via Glycoprotein 2 on Intestinal Microfold Cells for Cancer Immunotherapy, Nano Lett 25 (2025) 5165–5173. https://doi.org/10.1021/acs.nanolett.4c06123.
33. B. Yang, Y. Xu, W. Zhang, D. Zhu, B. Huang, Y. Yang, X. Jia, L. Feng, Oral absorption mechanisms of polysaccharides and potential as carriers for the construction of nano-delivery systems: A review, International Journal of Biological Macromolecules 310 (2025) 143184. https://doi.org/10.1016/j.ijbiomac.2025.143184.
34. J.S. Loh, W.Q. Mak, L.K.S. Tan, C.X. Ng, H.H. Chan, S.H. Yeow, J.B. Foo, Y.S. Ong, C.W. How, K.Y. Khaw, Microbiota-gut-brain axis and its therapeutic applications in neurodegenerative diseases, Signal Transduct Target Ther 9 (2024) 37. https://doi.org/10.1038/s41392-024-01743-1.
35. J. Liu, X. Zhang, Y. Liu, Z. Wu, Z. Cui, X. Pan, Y. Zheng, J. Wang, K. Wang, Y. Zhang, Intestinal lymphatic transport of Smilax china L. pectic polysaccharide via Peyer's patches and its uptake and transport mechanisms in mononuclear phagocytes, Carbohydr Polym 339 (2024) 122256. https://doi.org/10.1016/j.carbpol.2024.122256.
36. J.-K. Li, S. Veeraperumal, J.J. Aweya, Y. Liu, K.-L. Cheong, Fucoidan modulates gut microbiota and immunity in Peyer's patches against inflammatory bowel disease, Carbohydrate Polymers 342 (2024) 122421. https://doi.org/10.1016/j.carbpol.2024.122421.
37. Y. Hu, Y. He, Z. Niu, T. Shen, J. Zhang, X. Wang, W. Hu, J.Y. Cho, A review of the immunomodulatory activities of polysaccharides isolated from Panax species, J Ginseng Res 46 (2022) 23–32.

https://doi.org/10.1016/j.jgr.2021.06.003.

38. C. Lárez-Velásquez, F. López, Chito-oligosaccharides: A mini-review on sources, production, and agricultural applications, Ama 5 (2024) 2730. https://doi.org/10.54517/ama.v5i3.2730.
39. S. Xu, J. Shao, Z. Miao, H. Wang, H. Dai, B. Tian, R. Shi, Y. Zhong, C. Wang, Dual STING activation and CD47/SIRPα blockade via chitooligosaccharide-based nanoparticles to amplify antitumor immunity, Journal of Controlled Release 387 (2025) 114235. https://doi.org/10.1016/j.jconrel.2025.114235.
40. Y.-B. Miao, T. Xu, Y. Gong, A. Chen, L. Zou, T. Jiang, Y. Shi, Cracking the intestinal lymphatic system window utilizing oral delivery vehicles for precise therapy, J Nanobiotechnology 21 (2023) 263. https://doi.org/10.1186/s12951-023-01991-3.
41. Y. Zhang, M. Li, G. Du, X. Chen, X. Sun, Advanced oral vaccine delivery strategies for improving the immunity, Advanced Drug Delivery Reviews 177 (2021) 113928. https://doi.org/10.1016/j.addr.2021.113928.
42. W. Wang, C. Xue, X. Mao, Chitosan: Structural modification, biological activity and application, International Journal of Biological Macromolecules 164 (2020) 4532–4546. https://doi.org/10.1016/j.ijbiomac.2020.09.042.

Figures

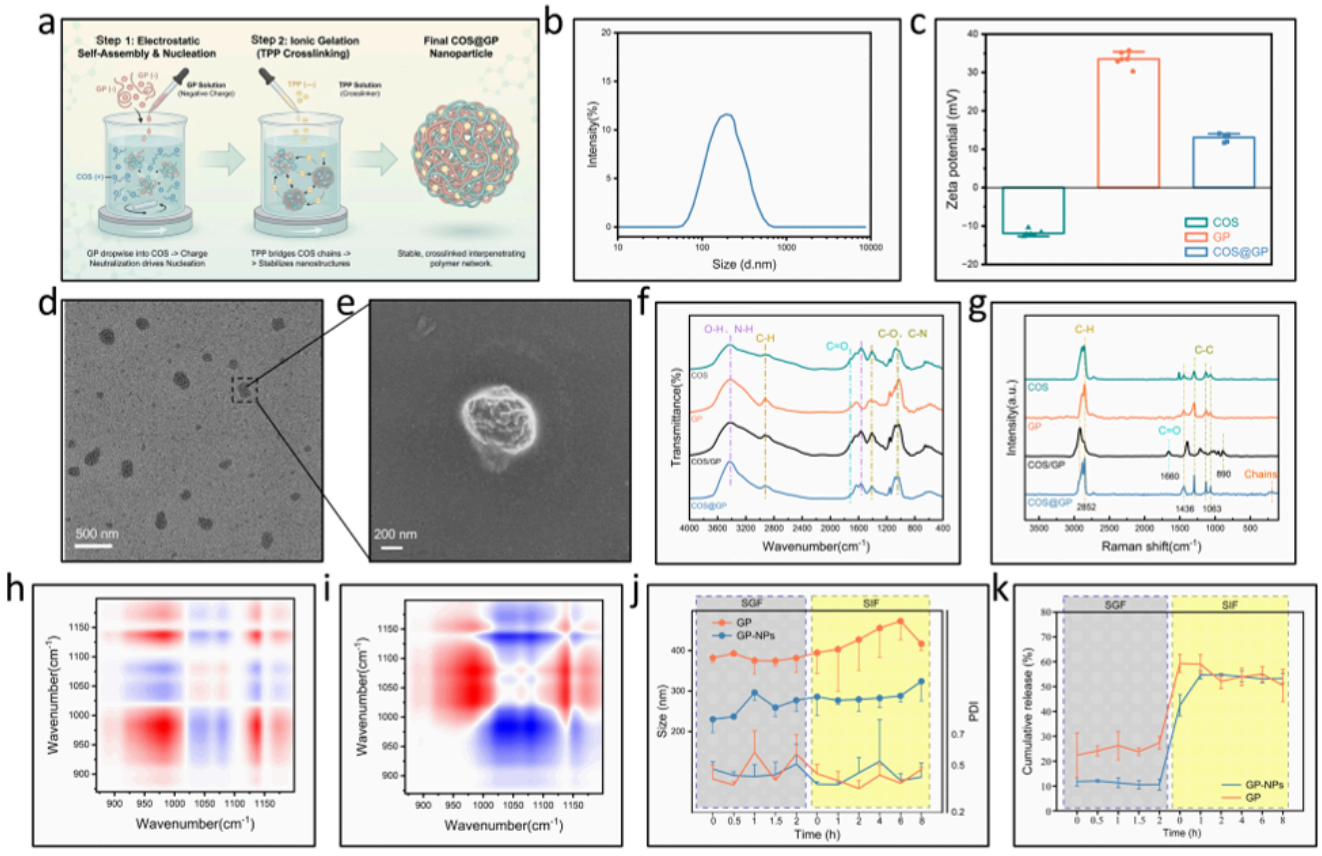


Figure 1

Preparation, characterization, and gastrointestinal stability of COS@GP. (a) Schematic of COS@GP self-assembly. Size (b) and zeta potential (c) of COS, GP, and COS@GP. TEM (d) and SEM (e) images of COS@GP. FT-IR (f) and Raman (g) spectra of COS, GP, and COS@GP. (h) 2D-FTIR synchronous (h) and asynchronous (i) maps of COS@GP (Red: positive; Blue: negative). Changes in particle size (j) and cumulative GP release (k) in SGF and SIF. Data are mean ± SD (n = 3).

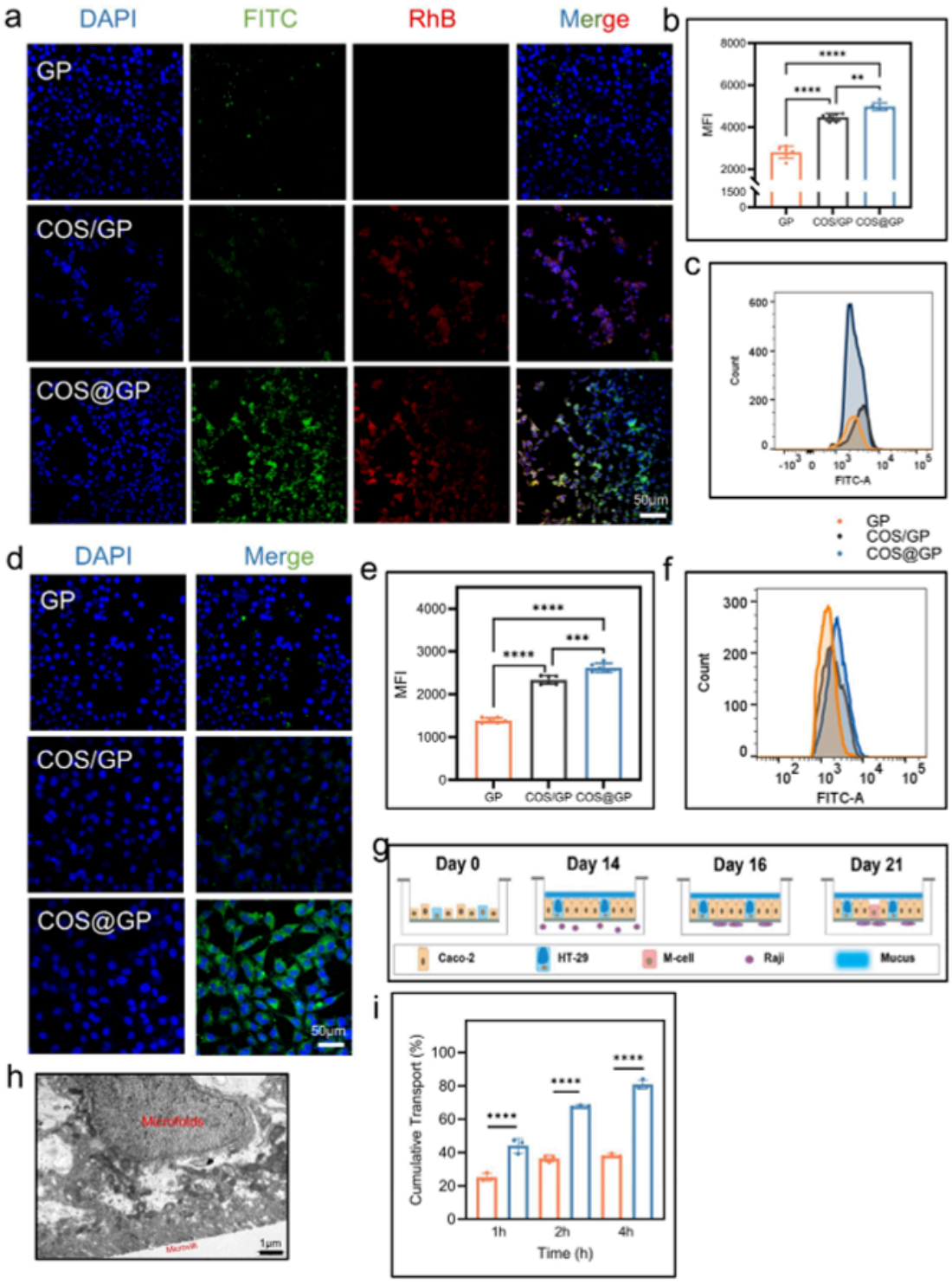


Figure 2

COS@GP nanoparticles enhance cellular internalization and facilitate M cell–mediated transcytosis. (a) Confocal images of cellular uptake in DC2.4 cells. (b) Quantification of MFI in DC2.4 cells. (c) Flow cytometry analysis of uptake in DC2.4 cells. (d) Confocal images of cellular uptake in 4T1 cells. (e) Quantification of MFI in 4T1 cells. (f) Flow cytometry analysis of uptake in 4T1 cells. (g) Schematic illustration of the *in vitro* M-cell co-culture model simulating the FAE. (h) SEM image of the M-cell model. (i) Cumulative transport percentage of GP and COS@GP across the M-cell model at predetermined time intervals (1, 2, and 4 h). **P < 0.01; ***P < 0.001; ****P < 0.0001.

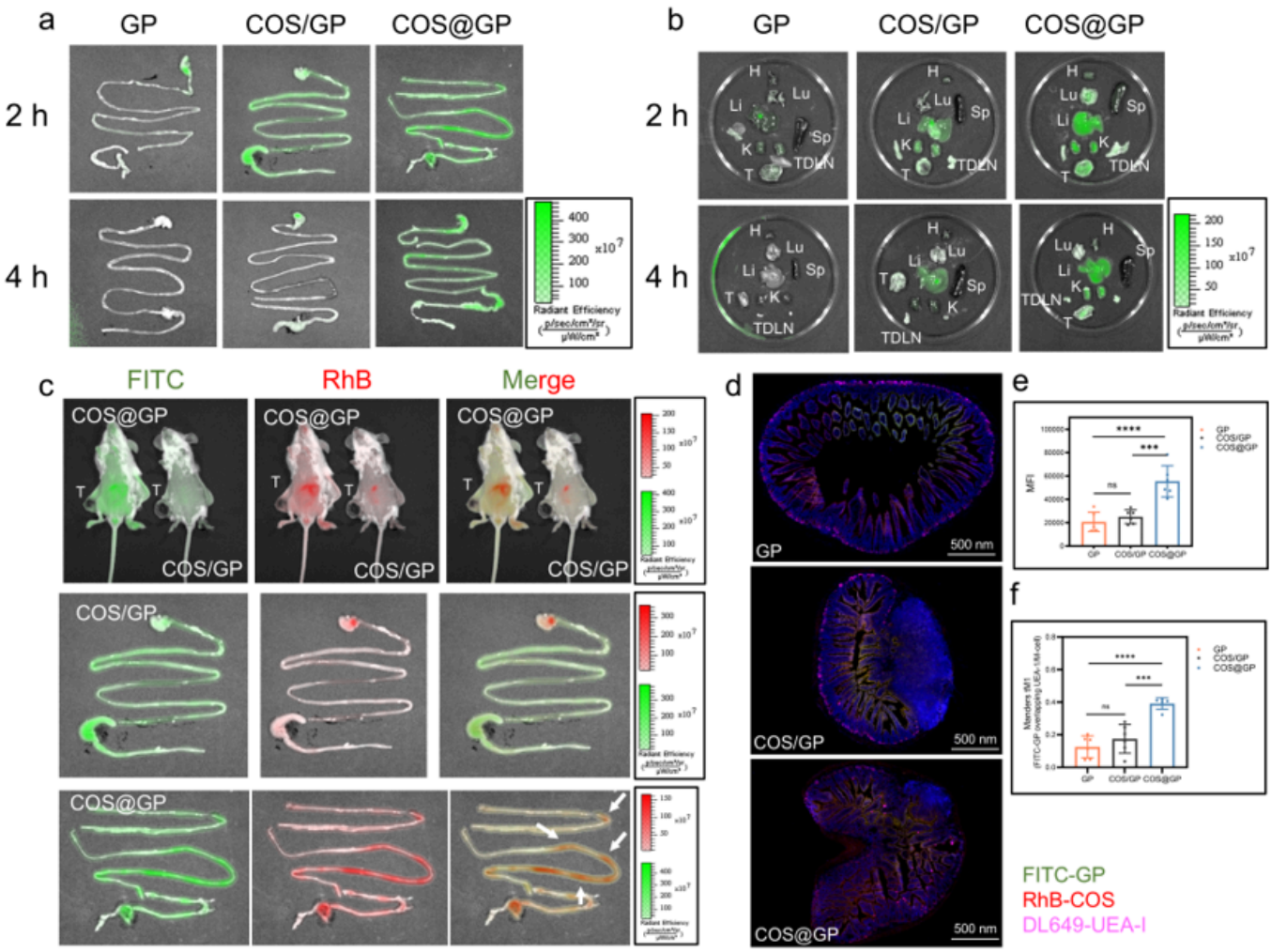


Figure 3

*Ex vivo*biodistribution and lymphatic targeting of different GP formulations. (a, b) Fluorescence images of (a) gastrointestinal tracts and (b) major organs at 2 h and 4 h post-oral administration. (c) Comparison of whole-body and *ex vivo* intestinal fluorescence distribution between COS/GP and COS@GP groups at 2 h. (d) Localization of FITC-GP (green) within the lymphoid follicles of Peyer's patches at 2 h. (e) Quantitative MFI of GP signals within Peyer's patches. (f) Structural integrity of COS@GP within intestinal tissues, quantified by Manders' colocalization coefficients. ns, not significant; ***P < 0.001; ****P < 0.0001.

Abbreviations: H, heart, Li, liver; Sp, spleen; Lu, lung; K, kidney; TDLN, tumor-draining lymph nodes; T, tumor.

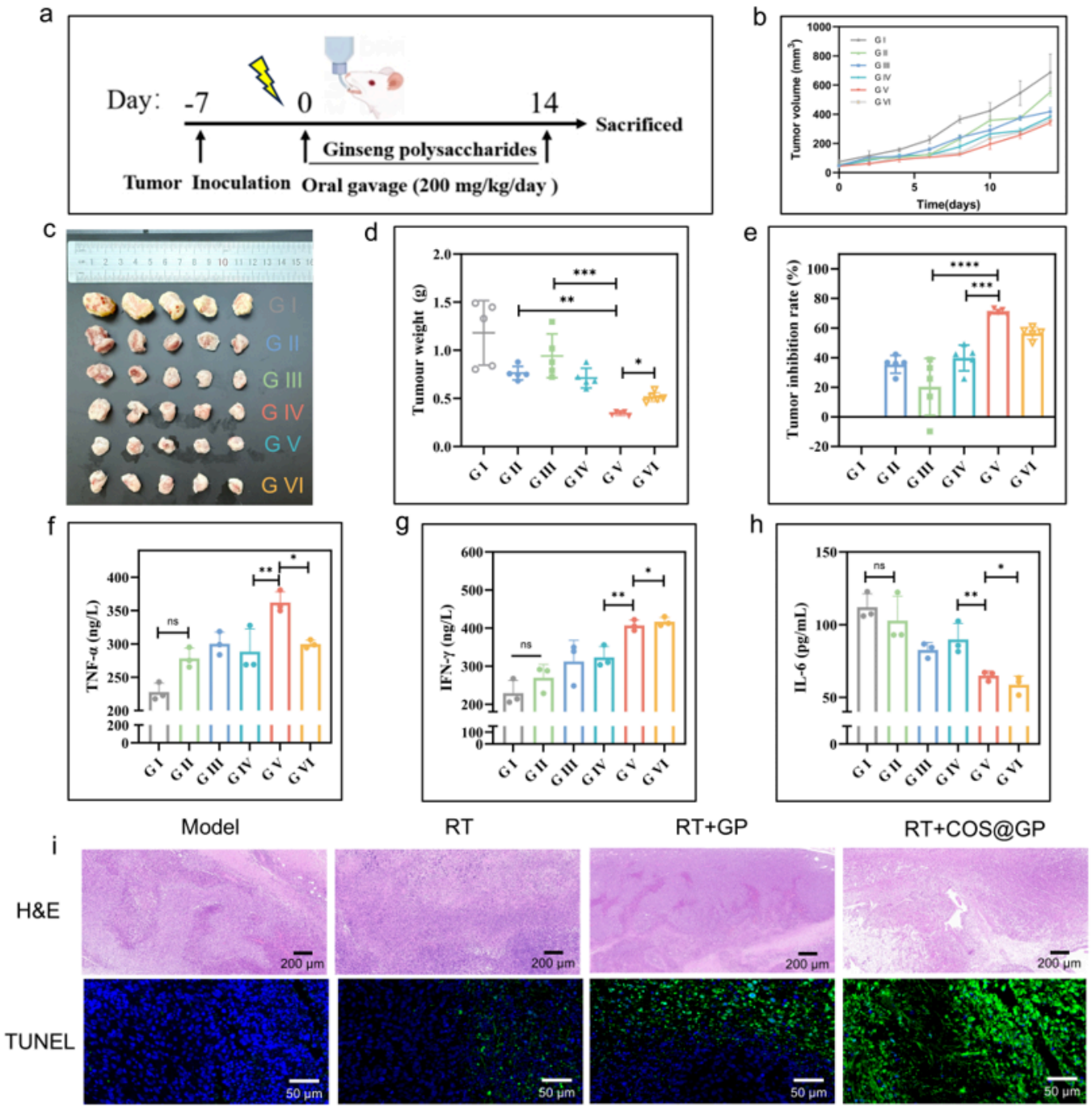


Figure 4

*In vivo*antitumor performance and immune remodeling effects of GP-based treatments combined with radiotherapy. (a) Experimental timeline and dosing regimen. (b) Tumor growth curves during treatment. (c) Representative photographs of excised tumors at the endpoint. (d) Tumor weights at sacrifice. (e) Tumor inhibition rates across groups. (f–h) Serum levels of TNF-α, IFN-γ, and IL-6 determined by ELISA. (i) Representative H&E and TUNEL staining of tumor sections. ns, not significant; *P < 0.05; **P < 0.01.

Abbreviations: G Ⅰ: Model, G Ⅱ: COS@GP, G Ⅲ: RT, G Ⅳ: RT+GP, G Ⅴ: RT+COS@GP, G Ⅵ: RT+COS@GP+FTY720.

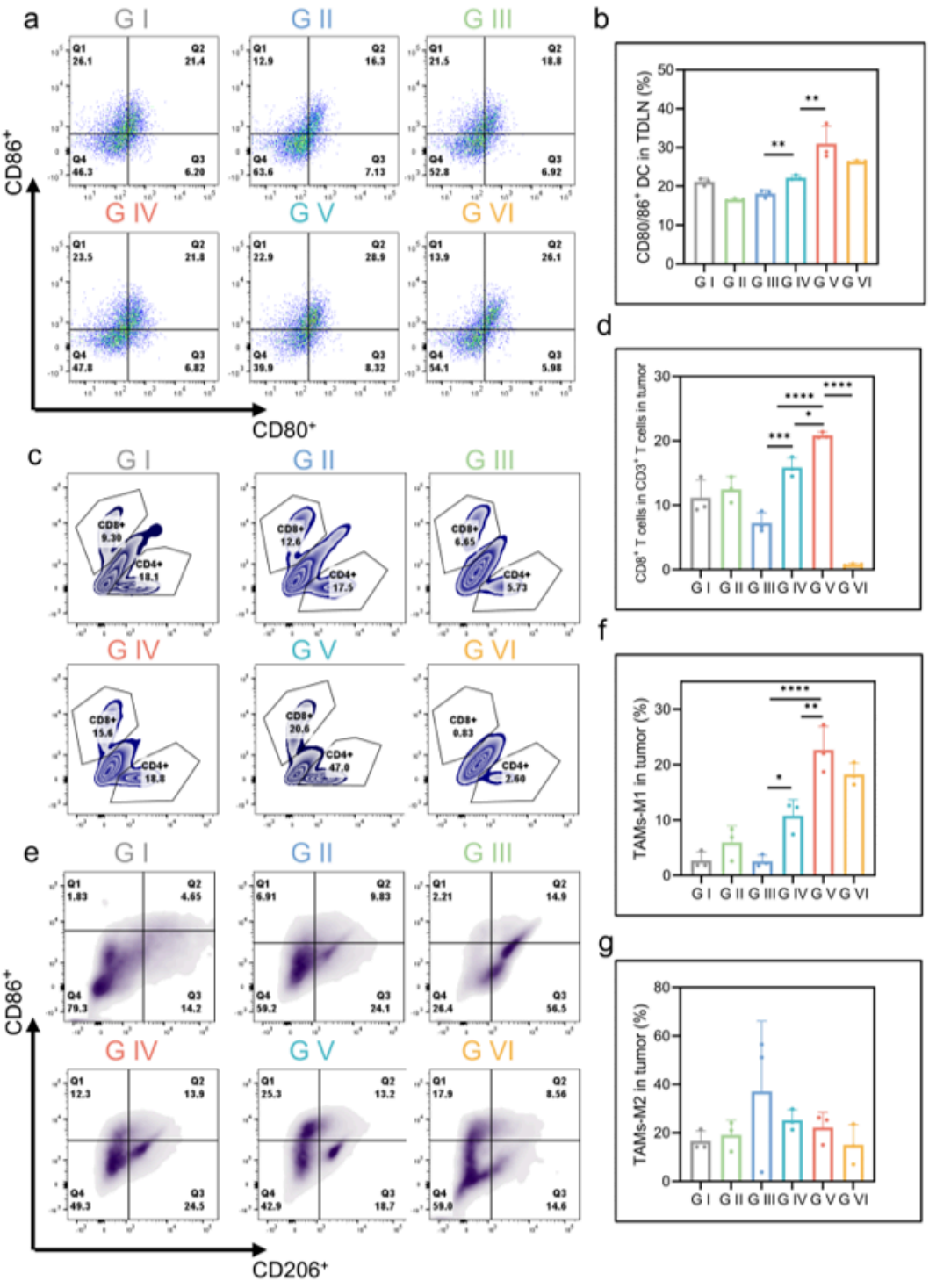


Figure 5

COS@GP enhances radiotherapy-driven immune activation by promoting DC maturation, effector T-cell infiltration, and macrophage repolarization *in vivo*. (a) Representative flow cytometric plots of CD80/CD86 expression on DC in TDLN. (b) Quantification of mature DC populations. (c) Flow cytometric

analysis of tumor-infiltrating effector T cells. (d) Quantification of $CD8^+$ T-cell infiltration. (e) Flow cytometric analysis of M1 and M2 macrophage phenotypes. (f–g) Quantitative analysis of macrophage polarization. *P < 0.05; **P < 0.01, ***P < 0.001; ****P < 0.0001.

Abbreviations: G □: Model, G □: COS@GP, G □: RT, G □: RT+GP, G □: RT+COS@GP, G □: RT+COS@GP+FTY720.

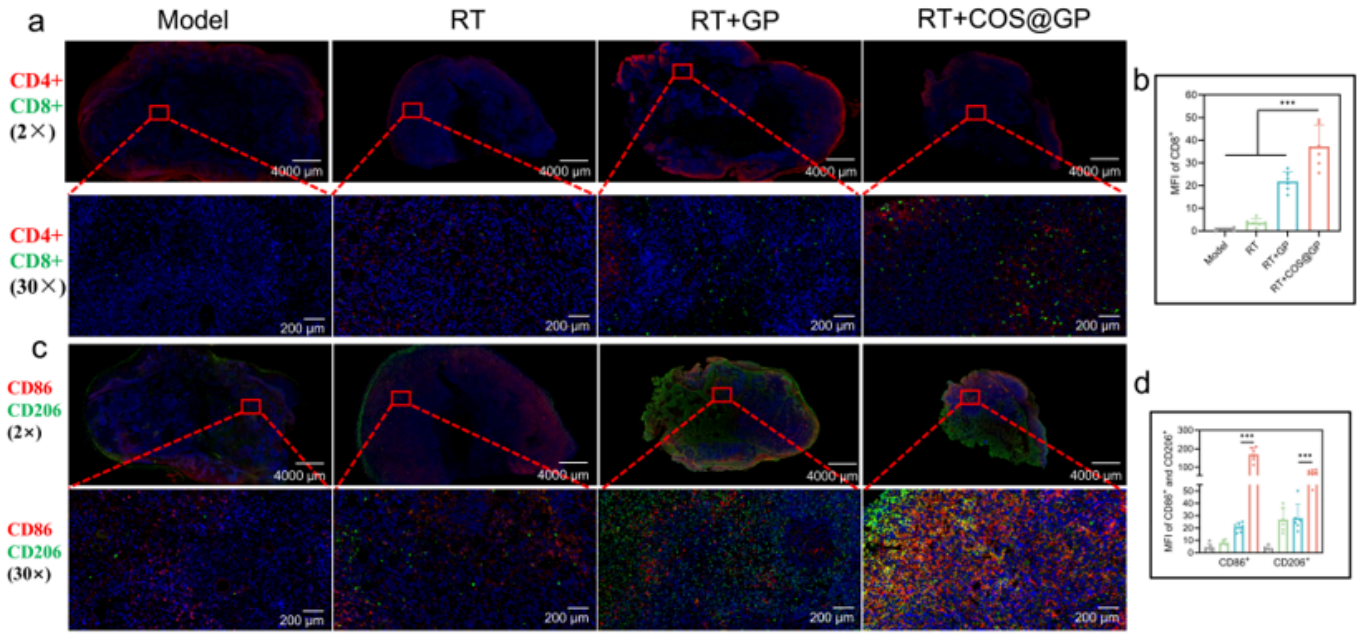


Figure 6

COS@GP combined with radiotherapy enhances antitumor immunity in the tumor microenvironment. (a) Representative immunofluorescence images of tumor-infiltrating T cells. (b) Quantification of $CD8^+$ T-cell infiltration (MFI). (c) Representative immunofluorescence images of tumor-associated macrophage polarization. (d) Quantification of CD86 and CD206 expression (MFI). ***P < 0.001

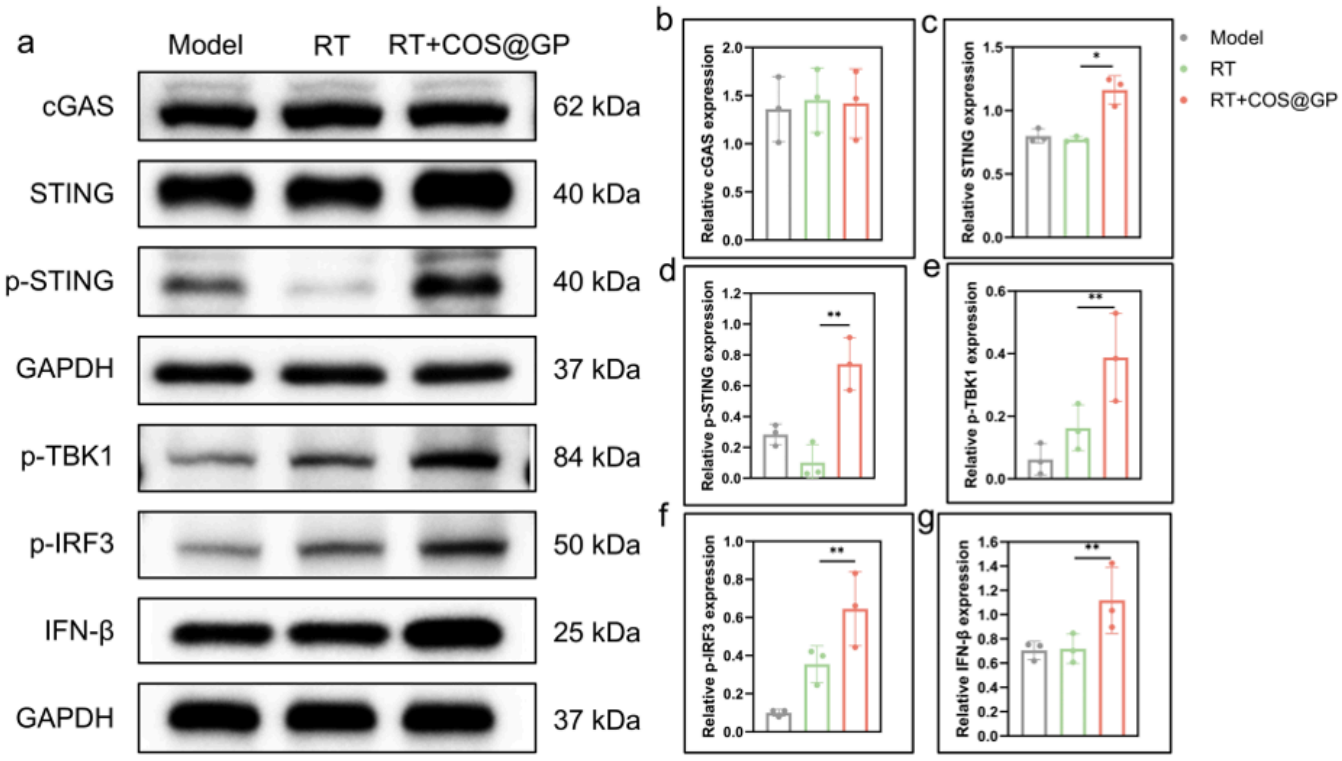


Figure 7

COS@GP enhances radiotherapy-induced activation of the cGAS–STING pathway. (a) Western blot analysis of cGAS–STING signaling proteins in tumor tissues. (b–g) Quantification of cGAS, STING, p-STING, p-TBK1, p-IRF3, and IFN-β protein expression. *P < 0.05; **P < 0.01.

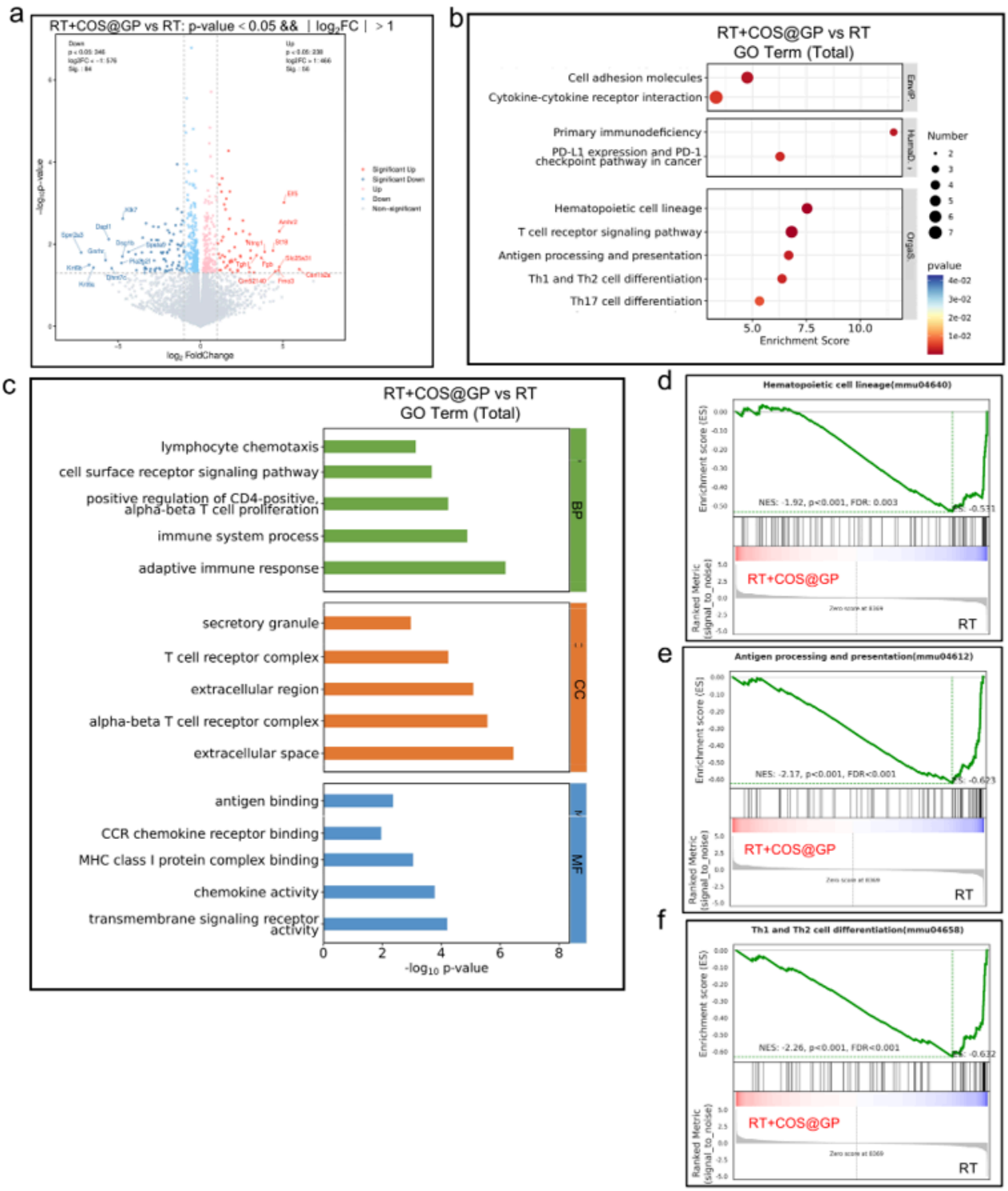


Figure 8

Transcriptomic profiling reveals immune pathway reprogramming following COS@GP treatment combined with radiotherapy. (a) Volcano plot of differentially expressed genes. (b) KEGG pathway enrichment analysis. (c) Gene Ontology (GO) enrichment analysis. (d-f) GSEA of immune-related pathways: (d) hematopoietic cell lineage, (e) antigen processing and presentation, and (f) Th1/Th2 cell differentiation.

Supplementary Files

This is a list of supplementary files associated with this preprint. Click to download.

- SupplementaryInformation.docx